Magnéli-like phases in epitaxial anatase TiO_2 thin films

R. Ciancio,[1,*] E. Carlino,[1] G. Rossi,[1,2] C. Aruta,[3] U. Scotti di Uccio,[3] A. Vittadini,[4,†] and A. Selloni[5]

[1]*CNR-IOM TASC, Area Science Park, Basovizza S.S. 14 Km 163.5, I-34149 Trieste, Italy*

[2]*Department of Physics, University of Milano, Via Celoria 16, I-20100 Milano, Italy*

[3]*CNR-SPIN and Dipartimento di Scienze Fisiche, Complesso Universitario di Monte S.Angelo, Via Cintia, I-80126 Napoli, Italy*

[4]*CNR-ISTM and CR-INSTM "Village," c/o Department of Chemical Sciences, University of Padua, Via Marzolo 1, I-35131 Padova, Italy*

[5]*Department of Chemistry, Princeton University, Princeton, NJ 08544, USA*

(Received 31 May 2012; revised manuscript received 6 September 2012; published 21 September 2012)

Using high-resolution transmission electron microscopy and image simulation techniques in combination with *ab initio* calculations, we show the existence of two different superlattices of crystallographic shear planes, analogous to the Magnéli phases of rutile, in oxygen-deficient films of anatase TiO_2 epitaxially grown on $LaAlO_3$ substrates. (103)- and (101)-oriented shear plane structures are detected in the outer film region and in proximity of the film/substrate interface, respectively. We show that these shear planes are characterized by TiO-like cubic local structures, which can deviate from the Ti_nO_{2n-1} stoichiometry of the classical rutile-derived Magnéli phases, particularly in the outer part of the film. Computed formation energies provide insights into the thermodynamic stability of the observed structures and their relations to the growth dynamics.

DOI: 10.1103/PhysRevB.86.104110 PACS number(s): 68.35.Dv, 68.37.Og, 68.55.−a, 71.15.Mb

I. INTRODUCTION

TiO_2 is an important technological material with a broad range of applications, including photocatalysis and solar energy conversion,[1] electrodes for electrochemical cells,[2] and novel memristor switching memories.[3] In particular, memristors are based on a resistive switching phenomenon which in TiO_2 has been associated to a local phase transformation to a Ti_nO_{2n-1} Magnéli phase (MP),[4,5] resulting from a reduction of the original TiO_2 matrix. The importance of this phenomenon and the fact that its basic mechanisms are not well understood[3] have prompted a renewed interest in the fundamental physical properties of MPs and, more generally, of reducing defects in TiO_2 and their behavior as a function of the oxygen nonstoichiometry.

It has long been known that TiO_2 can easily accommodate a wide range of substoichiometries. Within the rich titanium-oxygen phase diagram,[6] homologous series of compounds occur, among which the mixed-valence Ti_nO_{2n-1} Magnéli phases are important representatives. MPs can be described as resulting from a regular arrangement of crystallographic shear (CS) planes in oxygen-deficient rutile.[7,8] These structures are stable for intermediate stoichiometries between Ti_2O_3 and TiO_2 when the maximum amount of x in rutile TiO_{2-x} is larger than 10^{-4}. Diluted ($x < 10^{-4}$) oxygen vacancies form isolated point defects[9,10] which deeply affect the chemistry and photocatalytic activity of TiO_2.[11–13] With increasing concentration, oxygen vacancies rearrange to form CS planes. These rutile-derived MPs have been known for several decades and have been extensively characterized both experimentally and theoretically.[9,10,14–18] The occurrence and nature of CS structures in the other major TiO_2 polymorph, anatase, have not yet been established, even though their existence has been suggested previously for anatase thin films epitaxially grown on $LaAlO_3$ (LAO).[19] In view of the considerable interest of anatase films for new and/or improved technological applications,[20] a detailed characterization of their structure would be highly desirable, especially with regard to the nature and properties of reducing defects and their possible aggregation to form CS planes.

In this work, we use high-resolution transmission electron microscopy (HRTEM) experiments, HRTEM image simulation techniques, and density functional theory (DFT) calculations to characterize the structure and defects in LAO-supported TiO_2 anatase thin films. We show the existence of two different superlattices of CS planes analogous to the MPs derived from rutile and investigate the thermodynamic stability of these superstructures as a function of the oxygen supersaturation during film growth. Epitaxial TiO_2 thin-film materials are of considerable interest for their well-defined structural and compositional characteristics.[20] In particular, TiO_2/LAO stands out because the small lattice mismatch (approximately $\sim$0.2%)[21,22] in principle allows the realization of structurally excellent films with atomically sharp and clean film/substrate heterointerfaces. However, LAO-supported anatase films always contain defects whose nature and origin are unclear. In this context, high-resolution cross-sectional TEM provides a unique opportunity to ascertain the presence of structural defects at the atomic scale and to follow the evolution of shear structures across the growth direction.

II. METHODS

A. Sample and experiment

TiO_2 anatase films were deposited on (001)LAO substrates by pulsed laser deposition (KrF excimer laser, 248 nm) with a fluence of 2 J cm^{-2} at the target, 700 °C substrate temperature, and 10^{-1} mbar oxygen pressure at a rate of about 0.02 nm s^{-1} and monitored in situ by reflection high-energy electron diffraction (RHEED). Conventional x-ray diffraction analysis was routinely performed on the TiO_2/LAO films by a Philips X'Pert-XRD analytic diffractometer equipped with a four-circle cradle. A Cu $K\alpha$ ($\lambda = 1.5406$ Å) source was used at 40 kV and 40 mA. No secondary phases were detected in the TiO_2 films. Reciprocal space maps show the full in-plane matching between TiO_2 films and LAO substrate.

 ©2012 American Physical Society

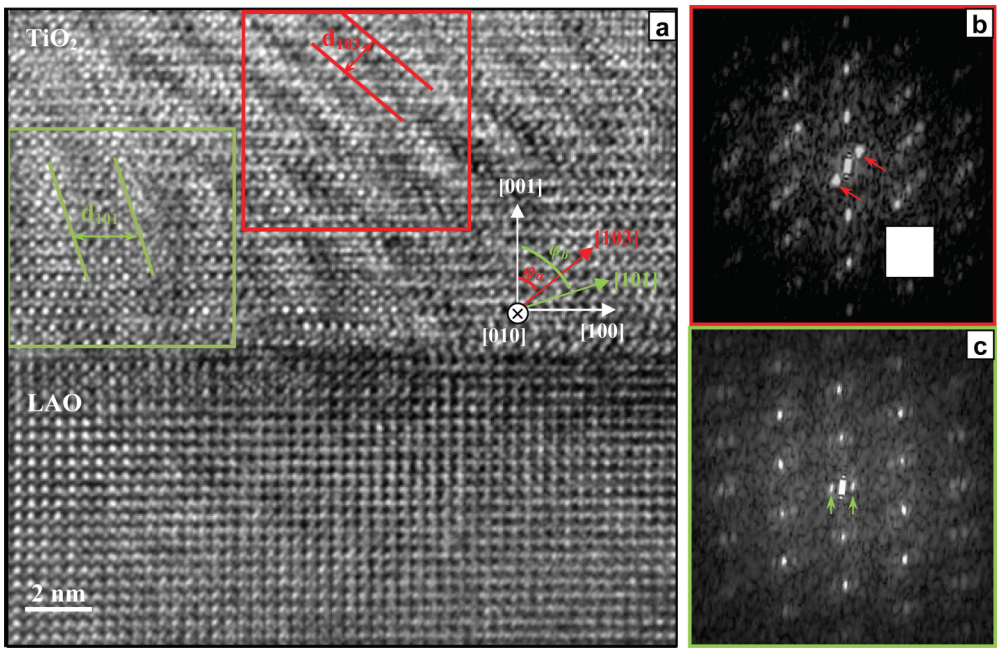

FIG. 1. (Color online) (a) HRTEM image of the TiO_2/LAO interfacial region taken in the [010] zone axis of the film. Diffractograms taken over the region containing (b) (103) and (c) (101) CS planes. The satellite peaks around the (000) reflection are indicated by arrows in the two diffractograms.

Cross-sectional TEM specimens in the [010] zone axis were prepared with a conventional polishing technique followed by dimpling and ion milling. TEM experiments were performed using a TEM/STEM JEOL 2010 UHR field emission gun microscope operated at 200 kV with a measured spherical aberration coefficient $C_s = 0.47 \pm 0.01$ mm. HRTEM image simulations were performed by JEMS.[23]

B. Theoretical approach

DFT calculations were performed using the Perdew-Burke-Ernzerhof[24] parametrization of the generalized gradient approximation (GGA), both without and with the inclusion of on-site Coulomb repulsion U on the Ti $3d$ states.[25] For the latter, the computed[26] value $U = 3.5$ eV was employed. We adopted the plane-wave pseudopotential scheme as implemented in the QUANTUM ESPRESSO package[27] with the computational setup extensively tested in Ref. 28. Brillouin-zone samplings were sufficiently dense to converge total energies to better than 1 meV/Ti atom. A 5-mRy "cold" smearing[28] was applied to populate the one-electron levels of metallic systems. Both the cell parameters and the internal ion coordinates were optimized with the Broyden-Fletcher-Goldfarb-Shanno (BFGS) algorithm (force threshold = 0.03 eV Å^{-1}, pressure tolerance = 50 bar). Finite-basis effects were corrected using the procedure by Bernasconi *et al.*[29] Preliminary runs were carried out without symmetry constraints, whereas the full cell symmetry was exploited in final calculations. Point defects were studied in nearly cubic $2\sqrt{2} \times 2\sqrt{2} \times 1$ supercells (32 TiO_2 units). For the GGA + U calculations, we used the GGA-optimized lattice constants but reoptimized the internal degrees of freedom. All the models were built and displayed using GDIS.[30]

The relative stabilities of systems with a variable stoichiometry (in our case TiO_x, with $1 < x < 2$) were investigated by *ab initio* thermodynamics.[31] Briefly, this approach allows the calculation of Gibbs free energies starting from DFT total energies. Similar calculations were previously performed for the Ti_nO_{2n-1} ($n = 3$–5) Magnéli phases in rutile by Liborio and Harrison.[17] A generic reduced X phase of Ti_nO_m stoichiometry can be seen as a defected TiO_2 system. The Gibbs formation energy of an oxygen defect of this phase can be defined as

$$\Delta G_X^f(T, p_{O_2}) = 1/n[G_X(T, p_{O_2}) - n g_{TiO_2}(T, p_{O_2}) + (2n - m)\mu_O(T, p_{O_2})], \quad (1)$$

where $\Delta G_X^f(T, p_{O_2})$ is the Gibbs energy of the X cell, $n g_{TiO_2}(T, p_{O_2})$ is the Gibbs energy of the bulk TiO_2 phase, and μ_O is the chemical potential of an O atom. By neglecting the pressure dependence of the free energies and chemical potentials of the condensed phases and assuming that the differences from vibrational contributions for these phases are also negligible, we obtain

$$\Delta G_X^f(T, p_{O_2}) 1/n[E_X - n E_{TiO_2} + (2n - m)\mu_O(T, p_{O_2})], \quad (2)$$

where for the condensed phases the free energies have been replaced by DFT total energies. The oxygen chemical potential $\mu_O(T, p_{O_2})$ can be expressed as

$$\mu_O(T, p_{O_2}) = \tfrac{1}{2} E_{O_2} + \Delta\mu_O(T, p_{O_2}), \quad (3)$$

where E_{O_2} is the total energy of O_2. Although $\Delta\mu_O$ can be explicitly calculated as a function of T,[17,32] here we simply use it as a free parameter containing all the temperature- and pressure-dependent free-energy contributions. $\Delta\mu_O$ can be varied between 0 (the dissociation limit of O_2) and $\frac{1}{2}\Delta H^f(TiO_2)$, the TiO_2 formation enthalpy, for which our computed value is −4.65 eV.

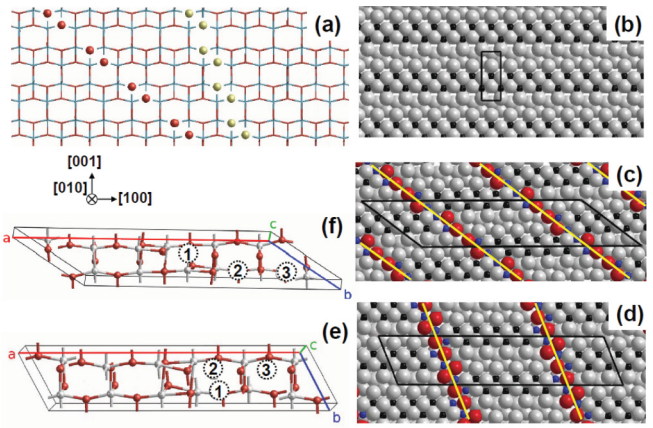

FIG. 2. (Color online) (a) Structural models for Magnéli-like phases in anatase. Clockwise from upper left (not to scale): (a) wire-frame model of the anatase-TiO_2 structure viewed down the [010] direction; the O atoms removed in the formation of a (103) and (101) CS plane are highlighted as red and yellow spheres, respectively. (b)–(d) Ball models of the anatase-TiO_2 structure and of the Ti_6O_{11} optimized superstructures formed by (103) and (101) CS planes, respectively. All structures are viewed down the [010] anatase direction. Yellow lines indicate CS planes, and black lines indicate the projected unit cell, i.e., the conventional body-centered tetragonal cell for anatase and the base-centered monoclinic cells for the superstructures. Large and small spheres are oxygen and titanium ions, respectively. Ions at the CS planes are shown in color to highlight the local structure: TiO (320)- and (210)-oriented thin films can be recognized in (c) and (d), respectively. (e)–(f) Ball-and-stick models of the triclinic primitive cells for the superstructures formed by (101) and (103) CS planes in (d) and (c), respectively. Triclinic cells are rotated for clarity, with the c axes of the cells aligned to the [010] anatase direction. Note the TiO-like cubic structure at the center of the cells. Large white spheres marked with numbers indicate some relevant sites for additional Ti interstitials; 1, 2, and 3 correspond to sites of decreasing stability.

III. RESULTS AND DISCUSSION

Figure 1(a) shows a HRTEM image of the TiO_2/LAO cross-sectional area taken with the electron beam parallel to the [010] direction of the film. The TiO_2 films are about 40 nm thick and form two adjacent slabs with the same Bravais lattice, compatible with the anatase tetragonal cell.[33] Film and substrate are well matched to each other, and the interface is straight and sharp. The film has a modulated structure with regular arrays of planar faults, characteristic of CS planes derived from oxygen deficiencies throughout the TiO_2 nanostructure. These planar faults exhibit a brighter contrast at the CS ridges with respect to the host matrix. At a closer inspection, two different groups of CS planes can be identified: majority CS planes have approximately 1.3-nm spacing and form an angle $\varphi_\alpha = 38^\circ$ with the [100] direction, whereas minority planes have ∼2.0 nm spacing and form an angle $\varphi_\beta = 68^\circ$ with [100]. The latter planes are only observed in proximity of the film/substrate interface. Diffractograms taken over the two CS regions and displayed in Figs. 1(b) and 1(c), respectively, show a typical multiple-peak pattern, which indicates a superstructure-like behavior originating from the CS planes in the film and defining two new superlattices. In each diffractogram, the distance between the spots [red and green arrows in Figs. 1(b) and 1(c), respectively] is strictly related to the 1.3- and 2.0-nm periodicity of the TiO_2-modulated structure. The arrowed peaks can thus be interpreted as satellite peaks of the d_{hkl} superlattices. The normal to the $(hkl)_A$ shear planes lies along the $c*$ direction of the new superlattices and is given, for a phase Ti_nO_{2n-1}, by the relation $c* = nd_{hkl}*$.

To elucidate the atomic structure of the film, several models were developed and optimized by means of DFT total-energy calculations in the generalized gradient approximation (GGA),[24] starting from geometries compatible with the CS plane density and orientation measured by HRTEM. In the Ti_nO_{2n-1} MPs of rutile,[34] CS planes are ideally obtained by removing layers of oxygen atoms of rutile and mutually displacing the resulting slabs by a $\frac{1}{2}[0\bar{1}1]$ vector. The resulting superstructures consist of periodically repeated corundum-like layers, with local Ti_2O_3 stoichiometry, sandwiched between rutile slabs, so that the overall stoichiometry is between TiO_2 and Ti_2O_3. For anatase, we built Ti_nO_{2n-1} Magnéli-like superstructures by removing (101) or (103) layers of O atoms [see Fig. 2(a)] and displacing half of the resulting anatase slabs by $\frac{1}{2}[010]$. Other models were constructed, e.g., by removing $(10\bar{2})$ layers of O atoms but turned out to be inconsistent with the experimental orientation. Structural modifications undergone by anatase [Fig. 2(b)] are best visualized with monoclinic cells (space group $B112$); see Figs. 2(c) and 2(d). As for the rutile MPs, the primitive cells are, however, triclinic (space group P_{-1}); see Figs. 2(e) and 2(f). The transformation matrices relating the monoclinic cells to the anatase unit cell are

$$M_{\{103\}} = \begin{bmatrix} 2n-1 & 0 & 0 \\ -3 & 0 & -1 \\ 0 & 1 & 0 \end{bmatrix}$$

and

$$M_{\{101\}} = \begin{bmatrix} 2n-1 & 0 & 0 \\ -1/2 & 0 & -1 \\ 0 & 1 & 0 \end{bmatrix},$$

with $n = 6$.

TABLE I. Optimized cell parameters for superstructures used to model the (103) crystal shear planes. The parameters refer to the primitive triclinic cell. The d_{CSP} parameter indicates the distance between consecutive shear planes.

Composition	a	b	c	α	β	γ	d_{CSP}
Ti_5O_9	18.148	7.760	3.860	75.60	83.89	137.96	10.86
Ti_6O_{11}	21.921	7.765	3.848	75.65	84.96	138.02	13.31
Ti_7O_{13}	25.090	7.808	3.826	75.82	85.63	135.82	16.22
Ti_6O_{11} + Ti@1	22.199	7.755	4.020	74.98	84.80	138.40	13.21

TABLE II. Optimized cell parameters for superstructures used to model the (101) crystal shear planes.

Composition	a	b	c	α	β	γ	d_{CSP}
Ti_5O_9	17.933	5.336	3.932	68.42	83.71	108.49	16.44
Ti_6O_{11}	21.675	5.405	3.861	69.07	84.89	108.43	20.02
Ti_7O_{13}	25.568	5.453	3.822	69.45	85.71	108.21	23.47
Ti_6O_{11} + Ti@1	21.675	5.541	3.940	69.16	84.84	108.87	19.95

Inspection of Figs. 2(e) and 2(f) reveals that the Ti atoms closest to the CS planes give rise to incipient TiO-like cubic structures, which can be described as $(320)_{TiO}$ and $(210)_{TiO}$ thin films for (103) and (101) CS planes, respectively. This suggests that the stoichiometry of the Magnéli-like phases of anatase can range from TiO_2 to TiO, thus reaching a higher degree of reduction with respect to the rutile-derived Ti_nO_{2n-1} phases. We computed the stability of the above-described Ti_nO_{2n-1} models for $n = 5$–7 as a function of the oxygen pressure by DFT-GGA calculations. The optimized unit cell parameters for all the investigated models are reported in Tables I and II. Each stoichiometry is found to have a narrow but finite stability interval (see Fig. 3), so the results of this analysis are not sufficient to identify which structure is actually observed in the experiment. Thus, we evaluated the models on a structural basis, by comparing the predicted spacings and orientations of the CS planes with the HRTEM experimental data. For both the (103) and the (101) CS planes, a very good agreement with the experiment is obtained for the $n = 6$ case ($d_{103} = 1.33$ nm, $\alpha = 37.6°$; $d_{101} = 2.05$ nm, $\beta = 69.1°$).

We notice that the (101) CS planes are predicted to be more stable than the (103) ones according to our DFT-GGA calculations (Fig. 3). This result is confirmed by calculations at the GGA + U level,[25] which are known to improve the description of the defect energetics in TiO_2 (Ref. 35; see Fig. 4). A higher stability of (101) CS planes is, however, not compatible with the predominance of (103) CS planes in the outer-film region observed in our TEM experiments. This discrepancy can be explained by a precipitation of Ti interstitials at the CS planes, leading to an enlargement of the TiO-like structure.[36] In agreement with previous theoretical studies on rutile,[17] we find that both O vacancies and Ti interstitials at regular bulk anatase sites either have positive formation energy or are unfavored with respect to CS planes at high concentrations (see Figs. 3 and 4). In contrast, Ti interstitials within CS planes, notably at the "1" sites of CS planes [see Figs. 2(e) and 2(f)], have negative formation energy; i.e., they tend to form spontaneously. In the presence of Ti interstitials within the CS planes, the (103)-oriented CS planes are stabilized with respect to the (101) ones and become largely favored over almost all the stability range of the CS plane structure (Fig. 4). The parameters of the Magnéli-like phase are only slightly perturbed by the presence of Ti interstitials and are still in excellent agreement with the experiment ($d_{103} = 1.32$ nm, $\alpha = 36.7°$). There is, however, a slight lattice expansion, increasing the mismatch with LAO. This mismatch was estimated from the difference, $\Delta[010]$, between the c parameter of the unit cells of the reduced phases and the theoretical lattice parameter, $a = 3.793$ Å, of LAO. (Note that all these parameters are related to the periodicity along the [010] direction of LAO, which is parallel to the interface; see Fig. 2.) The $\Delta[010]$ values calculated when the Ti interstitial is placed at the (103) and (101) planes are ∼6.2% and ∼4.1%, respectively. This suggests that the stabilization of (103) CS planes by Ti interstitials is hampered at the interface, where the epitaxial

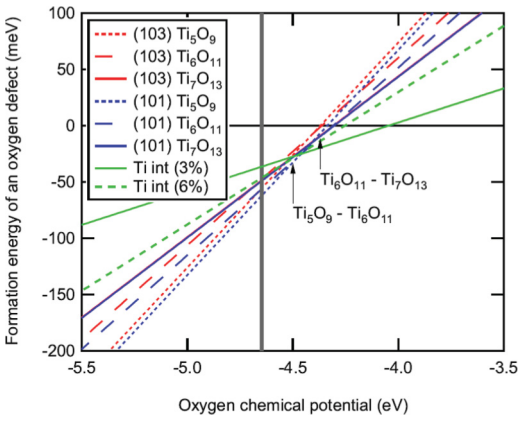

FIG. 3. (Color online) DFT-GGA formation energies for models corresponding to (103)- and (101)-oriented CS planes of different densities. Formation energies for Ti-interstitial point defects are shown for comparison. The grey vertical line marks the lower limit of the accessible chemical potential. The horizontal black line represents the formation energy.

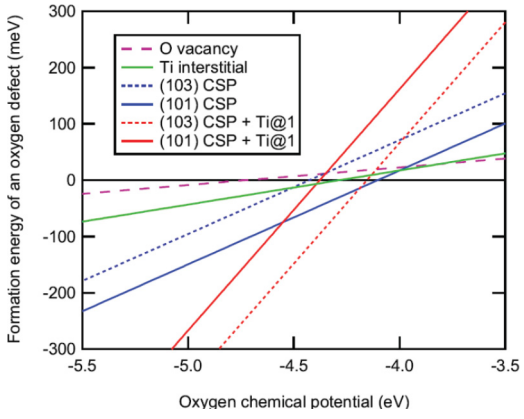

FIG. 4. (Color online) Computed (GGA + U) formation energy diagram of point defects and crystal shear planes (CSPs) in anatase TiO_2. Only CSPs corresponding to the experimentally observed geometries are considered. "Ti@1" indicates the presence of an additional Ti interstitial at the sites marked as "1" in Figs. 2(e) and 2(f), which changes the overall stoichiometry from Ti_6O_{11} to Ti_7O_{11}. Note the higher affinity to Ti interstitials of (103)-oriented CSPs. All the systems are antiferromagnetic, except the isolated Ti interstitial.

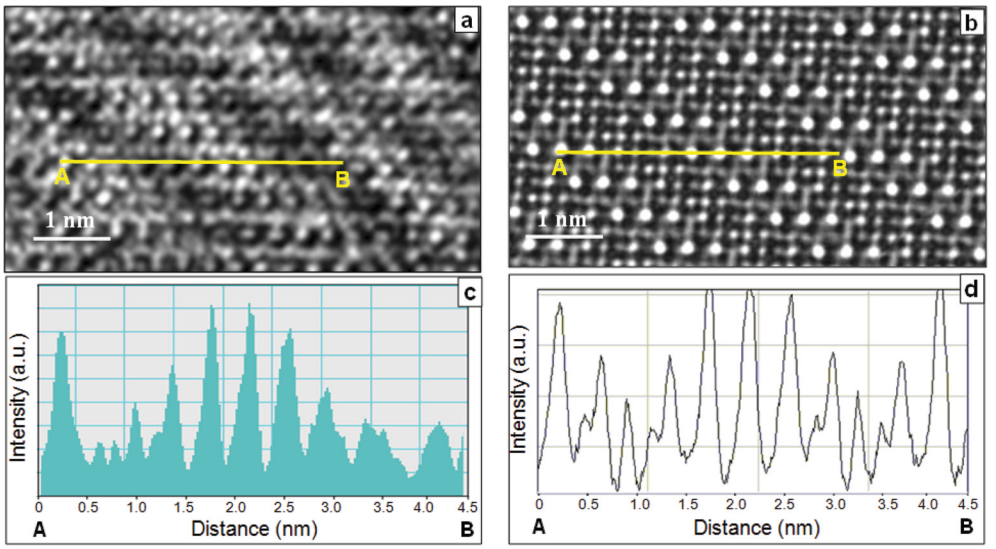

FIG. 5. (Color online) (a) HRTEM image focused at the film region containing (103) shear planes and taken in the [010] zone axis of the anatase film. (b) Simulated image obtained from the (103) CS modeled structure obtained at 6 nm thickness and 74-nm underfocus values. Line scans across image intensity maxima calculated along the yellow line of the (c) experimental and (d) simulated image.

constraints are stringent. Further support for this interpretation stems from the observation that the separation between the two shear regions coincides with the critical thickness, $L_c \sim 20$ nm, at which the growth mode of the TiO_2 films changes.[33] In other words, (103) CS planes can occur only when the film thickness exceeds L_c. This is consistent with results by Chambers *et al.*, who observed only (101) CS planes in TiO_2/LAO films[19] of thickness $l \sim 16$ nm, smaller than L_c.

We used the optimized structural models described above to simulate HRTEM images of the two CS regions directly comparable to the experimental ones. Figure 5(a) shows a HRTEM image focused at the (103) CS region. Through-focus/through-thickness series of images were calculated for a range of crystal thickness and TEM objective lens defocus values in the [001] zone axis of the modeled structures. By matching the characteristics of the experimental images with these simulations, it was possible to find the thickness/defocus window in which the details of the CS planes are reproduced by the simulation. The best image matching was obtained at 6 nm thickness and 74-nm underfocus values. The good agreement between the resulting simulated image [Fig. 5(b)] and the experimental one confirms that the structure of the film is well described by the theoretical model. The line profiles across the intensity maxima measured along the relevant segments in the experimental and simulated images are shown in Figs. 5(c) and 5(d), respectively.

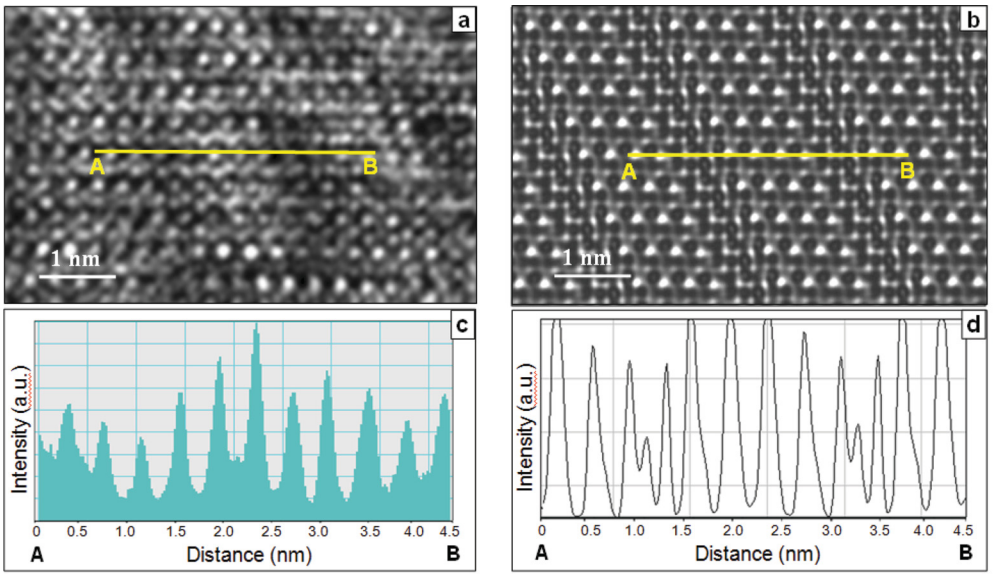

FIG. 6. (Color online) (a) HRTEM image focused at the film region containing (101) shear planes and taken in the [010] zone axis of the anatase film. (b) Image simulation calculated from the (101) CS modeled structure obtained at 6 nm thickness and 74-nm underfocus values. Line scans across phase maxima calculated along the yellow line of the (c) experimental and (d) simulated image.

The comparison between the HRTEM experimental image and the simulated image of the (101) CS model is shown in Fig. 6. Although the orientation and spacing of the (101) CS planes in the theoretical model agree with the experimental ones, a discrepancy is observed in the linear arrangement of the brighter contrast spots running along the long vector of the monoclinic model cell, which coincides with the [100] anatase direction. Indeed, line scan profiles taken across the intensity maxima in the simulated image show a discontinuous spacing between the bright contrast spots, whereas in the HRTEM image the intensity maxima constantly repeat over distances comparable to the long vector of the monoclinic cell. Such a discrepancy may be related to the Al interdiffusion between the substrate and the film region that was previously measured by high angle annular dark field scanning TEM and energy dispersive spectroscopy at the TiO_2/LAO interface.[33] The elucidation of the structure of the (101) CS region close to the interface would require, in addition to the work done for the pure phase, the determination of the density of Al impurities and their localization. This refinement goes beyond the purpose of this work and represents a challenge for future investigations.

IV. CONCLUSIONS

In conclusion, our HRTEM results on TiO_2/LAO show the existence of two different types of defective regions within the film nanostructure. By combining image simulations and calculations, we have demonstrated that both regions consist of defective phases of TiO_2 anatase, each characterized by shear planes with different crystallographic orientation and interstitial Ti inclusions. Their microstructure consists of alternate slabs of anatase and layers of TiO stoichiometry, which resemble the MPs of rutile. We have investigated the phase diagram of these structures as a function of the oxygen chemical potential and have provided an explanation for the relative predominance of (103) and (101) CS planes in the body of the film and close to the interface with the substrate, respectively. These results represent an important contribution towards the full elucidation of the atomic-scale structure of epitaxial anatase films. This understanding is essential for the control of the film quality and the optimization of manufacturing technologies based on such films.

ACKNOWLEDGMENTS

We are grateful to E. Cociancich for the assistance in the TEM specimen preparation. R.C.'s research activity has received funding from the European Community's Seventh Framework Programme 2007-2011 under grant agreement no. 212348 NFFA and Progetto strategico NFFA (fondi-MIUR). A.S. thanks the support of DoE-BES, Chemical Sciences, Geosciences and Biosciences Division, Contract No. DE-FG02-12ER16286.

*ciancio@iom.cnr.it
†andrea.vittadini@unipd.it

[1] M. Gratzel, Nature (London) **414**, 338 (2001).
[2] J. R. Smith and F. C. Walsh, J. Appl. Electrochem. **28**, 1021 (1998).
[3] K. Szot, M. Rogala, W. Speier, Z. Klusek, A. Besmehn, and R. Waser, Nanotechnology **22**, 254001 (2011).
[4] R. Waser and M. Aono, Nat. Mater. **6**, 833 (2007).
[5] D. H. Kwon *et al.*, Nat. Nanotechnol. **5**, 148 (2010).
[6] G. V. Samsonov, *The Oxide Handbook*, 2nd ed. (Plenum, New York, 1982).
[7] A. Magnéli, Pure Appl. Chem. **50**, 1261 (1978).
[8] J. M. Thomas, Eur. J. Solid State Inorg. Chem. **31**, 651 (1994).
[9] L. A. Bursill, B. G. Hyde, O. Terasaki, and D. Watanabe, Philos. Mag. **20**, 347 (1969).
[10] L. A. Bursill and B. G. Hyde, Philos. Mag. **23**, 3 (1971).
[11] M. A. Henderson, Surf. Sci. Rep. **66**, 185 (2011).
[12] K. Wakabayashi, Y. Yamaguchi, T. Sekiya, and S. Kurita, J. Lumin. **112**, 50 (2005).
[13] Y. He, O. Dulub, H. Cheng, A. Selloni, and U. Diebold, Phys. Rev. Lett. **102**, 106105 (2009).
[14] J. S. Anderson and R. J. D. Tilley, J. Solid State Chem. **2**, 472 (1970).
[15] L. A. Bursill and M. G. Blanchin, J. Solid State Chem. **51**, 321 (1984).
[16] I. Leonov, A. N. Yaresco, V. N. Antonov, U. Schwingenschlogl, V. Eyert, and V. I. Anisimov, J. Phys. Condens. Matter **18**, 10955 (2006).
[17] L. Liborio and N. Harrison, Phys. Rev. B **77**, 104104 (2008).
[18] L. Liborio, G. Mallia, and N. Harrison, Phys. Rev. B **79**, 245133 (2009).
[19] S. A. Chambers *et al.*, Thin Solid Films **418**, 197 (2002).
[20] S. A. Chambers, Adv. Mater. **22**, 219 (2010).
[21] M. Y. Murakami *et al.*, Appl. Phys. Lett. **78**, 2664 (2001).
[22] R. J. Kennedy and P. A. Stampe, J. Cryst. Growth **252**, 333 (2003).
[23] P. Stadelmann (2006) JEMS Electron Microscopy Software, JAVA version 3.0505W2006, http://cimewww.epfl.ch/people/stadelmann/jemsWebSite/jems.html.
[24] J. P. Perdew, K. Burke, and M. Ernzerhof, Phys. Rev. Lett. **77**, 3865 (1996).
[25] V. I. Anisimov, J. Zaanen, and O. K. Andersen, Phys. Rev. B **44**, 943 (1991).
[26] M. Cococcioni and S. de Gironcoli, Phys. Rev. B **71**, 035105 (2005).
[27] P. Giannozzi *et al.*, J. Phys. Condens. Matter **21**, 395502 (2009).
[28] N. Marzari, D. Vanderbilt, A. De Vita, and M. C. Payne, Phys. Rev. Lett. **82**, 3296 (1999).
[29] M. Bernasconi, G. L. Chiarotti, P. Focher, S. Scandolo, E. Tosatti, and M. Parrinello, J. Phys. Chem. Solids **56**, 501 (1995).
[30] S. Fleming and A. Rohl, Z. Kristallogr. **220**, 580 (2005).
[31] K. Reuter and M. Scheffler, Phys. Rev. B **65**, 035406 (2001).
[32] B. J. Morgan and G. W. Watson, J. Phys. Chem. C **114**, 2321 (2010).
[33] R. Ciancio, E. Carlino, C. Aruta, D. Maccariello, F. Miletto Granozio, and U. Scotti di Uccio, Nanoscale **4**, 91 (2012).
[34] L. A. Bursill and B. G. Hyde, Prog. Solid State Chem. **7**, 177 (1972).
[35] C. Di Valentin, G. Pacchioni, and A. Selloni, J. Phys. Chem. C **113**, 20543 (2009).
[36] We also performed test calculations in which the experimental features classified as CS planes were modeled as planar aggregates of Ti interstitials. However, HRTEM simulations based on such models showed a poor agreement with the experiment.